Korean Journal of Remote Sensing, Vol.21, No.1, 2005, pp.59~72

InSAR Studies of Alaska Volcanoes

Zhong Lu*, Chuck Wicks, Dan Dzurisin***, and John Power******

U.S. Geological Survey (USGS), EROS Data Center, SAIC, U.S.A*
USGS, Earthquake & Volcano Hazards Programs, U.S.A**
USGS, Cascades Volcano Observatory, U.S.A***
USGS, Alaska Volcano Observatory, U.S.A****

Abstract : Interferometric synthetic aperture radar (InSAR) is a remote sensing technique capable of measuring ground surface deformation with sub-centimeter precision and spatial resolution in tens-of-meters over a large region. This paper describes basics of InSAR and highlights our studies of Alaskan volcanoes with InSAR images acquired from European ERS-1 and ERS-2, Canadian Radarsat-1, and Japanese JERS-1 satellites.

Key Words : Synthetic Aperture Radar (SAR), Interferometric SAR (InSAR), Ground Surface Deformation, Volcano Geodesy.

1. Introduction

Interferometric synthetic aperture radar (InSAR) imaging is a recently developed remote sensing technique. The term "interferometry" draws its meaning from two root words: interfere and measure. The interaction of electromagnetic waves, referred to as interference, is used to precisely measure distances and angles. Interference of electromagnetic waves that are transmitted and received by a synthetic aperture radar (SAR), an advanced imaging radar instrument, is called interferometric SAR (InSAR). Very simply, InSAR involves the use of two or more SAR images of the same area to extract the land surface topography and its deformation patterns.

InSAR is formed by interfering signals from two spatially or temporally separated antennas. The spatial separation of the two antennas is called the baseline. The two antennas may be mounted on a single platform for simultaneous interferometry, the usual implementation for aircraft and spaceborne systems such as Topographic SAR (TOPSAR) and Shuttle Radar Topography Mission (SRTM) systems (Zebker *et al.*, 1992; Farr and Kobrick, 2000). Alternatively, InSAR can be created by utilizing a single antenna on an airborne or spaceborne platform in nearly identical repeating orbits for repeat-pass interferometry (Gray and Farris-Manning, 1992). For the latter case, even though the antennas do not illuminate the same area at the same time, the two sets of signals recorded during the two passes will be highly correlated if the scattering properties of the ground surface are undisturbed between viewings. This is the typical implementation for spaceborne sensors such as the U.S. SEASAT, European Remote-sensing Satellites

Received 10 December 2004; Accepted 20 January 2005.

(ERS-1 and ERS-2), Shuttle Imaging Radar-C/L (SIR-C/L), Canadian Radar Satellite (Radarsat-1), Japanese Earth Resources Satellite (JERS-1), European Environmental Satellite (Envisat), all of which operate at wavelengths ranging from a few centimeters (C-band) to tens of centimeters (L-band) (Table 1). It is this configuration that makes InSAR capable of measuring ground-surface deformation with centimeter to subcentimeter precision at a spatial resolution of tens-of-meters over a relatively large region (~10^4 km^2).

The capability of measuring land surface deformation using repeat-pass InSAR data was first demonstrated by Gabriel *et al.* (1989). However, it is not until 1993 when Massonnet *et al.* (1993) published the discovery of mapping earthquake displacement from ERS-1 InSAR data that the science community enthusiastically began to embrace InSAR technology. Two years later, Massonnet *et al.* (1995) were also the first to apply ERS-

Table 1. Spaceborne SAR Sensors capable of deformation mapping.

Mission	Agency	Period of Operation[1]	Orbit Repeat Cycle	Frequency	Wave-length	Incidence Angle at Swath Center	Resolution
Seasat	NASA[2]	06/27-10/10, 1978	17 days	L-band 1.2 GHz	25 cm	20 to 26 degrees	25 m
ERS-1	ESA[3]	07/1991 to 03/2000	3, 168, and 35 days[4]	C-band 5.3GHz	5.66 cm	23 degrees	30 m
SIR-C/X-SAR	NASA, DLR[5], ASI[6]	04/09-04/20, 1994, and 09/30 to 10/11, 1994	6-month, 1-, 2-, 3-day[7]	L-band 1.249 GHz C-band 5.298 GHz X-band 9.6 GHz	24.0 cm 5.66 cm 3.1 cm	17 to 63 degrees (L- and C-band) 54 degrees (X-band)	10 to 200 m (30 m typical)
JERS-1	JAXA[8]	02/1992 - 10/1998	44 days	L-band 1.275GHz	23.5 cm	39 degrees	20 m
ERS-2	ESA	04/1995 to present	35 days	5.3 GHz	5.66 cm	23 degrees	30 m
Radarsat-1	CSA[9]	11/1995 to present	24 days	C-band 5.3 GHz	5.66 cm	10 to 59 degrees	10-100 m
Envisat	ESA	03/2002 to present	35 days	C-band 5.331 GHz	5.63 cm	14 to 45 degrees	20-100 m
ALOS	JAXA	Planned launch in late 2005	46 days	L-band 1.275 GHz	23.5 cm	8 to 60 degrees	10-100 m

[1] Information was current in September 2004.

[2] National Aeronautics and Space Agency

[3] European Space Agency

[4] To accomplish various mission objectives, the ERS-1 repeat cycle was 3 days from July 25, 1991 to April 1, 1992 and from December 23, 1993 to April 9, 1994, 168 days from April 10, 1994 to March 20, 1995, and 35 days at other times.

[5] German Space Agency

[6] Italian Space Agency

[7] During day 3-4 of the second mission, SIR-C/X was commanded to retrace the flight path of the first mission to acquire repeat-pass InSAR data with a six-month time separation. From day 7 to the end of the second flight, the shuttle was commanded to repeat the flight path of the previous days to acquire 1-day, 2-day, and 3-day repeat-pass InSAR data.

[8] Japan Aerospace Exploration Agency

[9] Canadian Space Agency

1 InSAR imagery to map the volcanic deformation associated with the eruption of Etna volcano. Today, scientists use InSAR data to study volcanoes worldwide.

2. Basics of Interferometric SAR (InSAR)

A SAR transmits electromagnetic waves at a wavelength ranging from a few millimeters to a few meters. The radar wave propagates through the atmosphere and interacts with the Earth surface. Part of the energy is returned back and recorded by the SAR. Using a sophisticated image processing technique, called SAR processing (Curlander and McDonough, 1991), both the intensity and phase of the reflected (or backscattered) signal of each ground resolution element (a few meters to tens of meters) can be calculated. So, essentially, a complex-valued SAR image represents the reflectivity of the ground surface. The amplitude or intensity of the SAR image (Fig. 1a) is primarily controlled by terrain slope, surface roughness, and dielectric constants, whereas the phase of the SAR image (Fig. 1b) is primarily controlled by the distance from satellite antenna to ground targets and partially controlled by the atmospheric delays as well as the interaction of electromagnetic waves with ground surface (Fig. 1).

To generate an interferogram requires two single-look-complex (SLC) SAR images. Neglecting phase shifts induced by the transmitting/receiving antenna and SAR processing algorithms, the phase value of a pixel in a SLC SAR image (Fig. 1b) can be represented as

$$\phi_1 = -\frac{4\pi}{\lambda} r_1 + \varepsilon_1 \qquad (1)$$

where r_1 is the apparent range distance (including possible atmospheric delay) from the antenna to the ground target, λ is the SAR wavelength of radar, and ε_1 is the sum of phase shift due to the interaction between

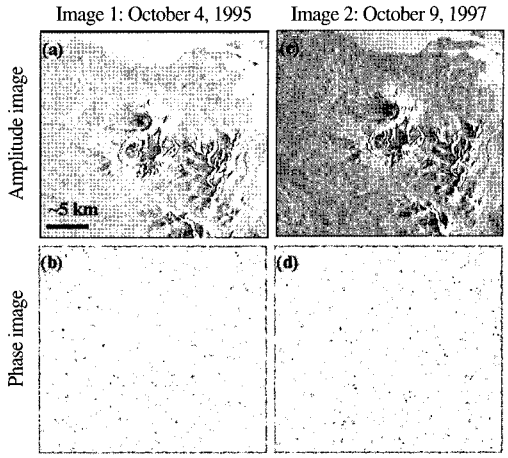

Fig. 1. Two SLC SAR images that were acquired on October 4, 1995 by ERS-1 satellite and on October 9, 1997 by ERS-2 satellite over the Mount Peulik volcano, Alaska. The amplitude and phase of each SAR image are shown separately. The amplitude of a SAR image is primarily controlled by terrain slope, surface roughness and dielectric constants while the phase value of each pixel is related to the apparent distance from the satellite to the ground target.

the incident radar wave and scatterers within the resolution cell. Because the backscattering phase (i.e., ε_1) is a randomly distributed (unknown) variable, the phase value (ϕ_1) in a single SAR image cannot be used to calculate the range information (r_1) and is of no practical use. However, a second SLC SAR image (Fig. 1c+1d) could be obtained over the same area at a different time with a phase value of

$$\phi_2 = -\frac{4\pi}{\lambda} r_2 + \varepsilon_2 \qquad (2)$$

Note that phase values in the second SAR image cannot provide range information (i.e., r_2) either.

An interferogram is created by co-registering two SAR images and differencing the corresponding phase values of the two SAR images on a pixel-by-pixel basis (Fig. 2). The phase value of the resulting interferogram is

$$\phi = \phi_1 - \varphi_2 = -\frac{4\pi(r_1 - r_2)}{\lambda} + (\varepsilon_1 - \varepsilon_2) \qquad (3)$$

The fundamental assumption in repeat-pass InSAR is

that the scattering characteristics of the ground surface remains undisturbed. The degree of changes in backscattering characteristics can be quantified by the interferometric coherence. Assuming that the interactions between the radar waves and scatterers remain the same when the two SAR images were acquired (i.e., $\varepsilon_1 = \varepsilon_2$), the interferometric phase value can be expressed

$$\phi = -\frac{4\pi(r_1 - r_2)}{\lambda} \quad (4)$$

Nominal values for the range difference, $(r_1 - r_2)$, extend from a few meters to several hundred meters. The SAR wavelength (i.e., λ) is of the order of several centimeters. Because the measured interferometric phase value (i.e., ϕ) ranges from $-\pi$ to π, there is an ambiguity of many cycles (i.e., numerous 2π values) in the interferometric phase value. Therefore, the phase value of a single pixel in an interferogram is of no practical use. However, the change in range difference, $\delta(r_1 - r_2)$, between two neighboring pixels that are a few meters apart, is normally much smaller than the SAR wavelength. So the phase difference between two nearby pixels, $\delta\phi$, can be used to infer the range distance difference (i.e., $r_1 - r_2$) to a sub-wavelength precision. This explains how InSAR uses the phase difference to infer the change in range distance to an accuracy of centimeters or millimeters.

The phase (or range distance difference) in the interferogram represented by Equation 4 and exemplified by Fig. 2 contains contributions from both the topography and any possible ground surface deformation. Therefore, the topographic contribution needs to be removed to derive a deformation map. The most commonly used procedure is to use an existing digital elevation model (DEM) and the InSAR imaging geometry to produce a synthetic interferogram and subtract it from the interferogram to be studied (Massonnet and Feigl, 1998; Rosen *et al.*, 2000; Hanssen, 2001). This is the so-called 2-pass InSAR. Alternatively, the synthetic interferogram that represents topographic contribution can come from a different interferogram of the same area. The procedures are then called 3-pass, or 4-pass InSAR (Zebker *et al.*, 1994). We now briefly explain how to simulate the topographic effect based on an existing DEM to derive a deformation map in the 2-pass InSAR.

Two steps are required to simulate a topography-only interferogram based on a DEM. First, the DEM needs to be resampled to project heights from a map coordinate into the appropriate radar geometry via geometric simulation of the imaging process. The InSAR imaging geometry is shown in Fig. 3. The InSAR system acquires two images of the same scene with SAR platforms located at A_1 and A_2. The baseline, defined as the vector from A_1 to A_2, has a length B, and is tilted with respect to the horizontal by an angle α. The slant range r from the SAR to a ground target T with a elevation value h is proportional to the measured phase values in the SAR images by Equations 1 and 2. The look angle from A_1 to the ground point T is θ_1. For each ground resolution cell at ground range r_g with elevation h, the slant range value (r_1) should satisfy

$$r_1 = \sqrt{(H+R)^2 + (R+h)^2 - 2(H+R)(R+h)\cos(\frac{r_g}{R})} \quad (5)$$

where H is the satellite altitude above a reference earth surface which is assumed to be a sphere with a radius R. The radar slant range and azimuth coordinates are calculated for each point in the DEM. This set of coordinates forms a non-uniformly sampled grid in the SAR coordinate space. The DEM height data are then resampled into a uniform grid in the radar coordinates using the values over the non-uniform grid.

Second, the precise look angle from A_1 to ground target T at ground range r_g, slant range r_1 and elevation h is calculated:

$$\theta_1 = \arccos\left[\frac{(H+R)^2 + r_1^2 - (R+h)^2}{2(H+R)r_1}\right] \quad (6)$$

By knowing θ_1, the interferometric phase value due to the topographic effect at target T can be calculated,

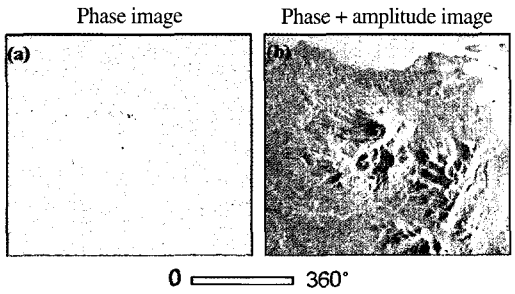

Fig. 2. An interferogram is formed by differencing the phase values of two SAR images (Figures 1b and 1d) which have been co-registered. The resulting interferogram contains fringes produced by the differing viewing geometries, topography, any atmospheric delays, and surface deformation. The perpendicular component of the baseline is 35 m. Each interferometric fringe (full color cycle) represents 360° of phase change (or 2.83 cm of range change between the ground and the satellite).

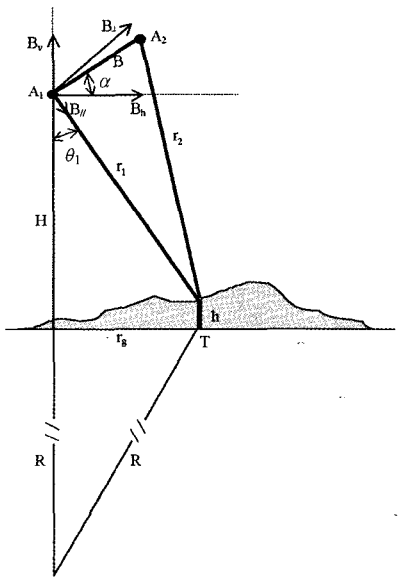

Fig. 3. InSAR imaging geometry. The InSAR system acquires two images of the same scene with SARs located at A_1 and A_2. The spatial distance between A_1 and A_2 is called the baseline, which has length B, and is tilted with respect to the horizontal by α. The baseline B can be expressed by a pair of horizontal (B_h) and vertical (B_v) components, or a pair of parallel ($B_{//}$) and perpendicular ($B_\perp$) components. The range distances from the SARs to a ground target T with elevation h are r_1 and r_2, respectively. The look angle from A_1 to the ground point T is θ_1.

$$\phi_{dem} = -\frac{4\pi}{\lambda}(r_1 - r_2)$$

$$= \frac{4\pi}{\lambda}\left(\sqrt{r_1^2 - 2(B_h \sin\theta_1 - B_v \cos\theta_1)r_1 + B^2} - r_1\right) \quad (7)$$

where B_h and B_v are horizontal and vertical components of the baseline B (Fig. 3).

Fig. 4 shows the simulated topographic effect in the interferogram in Fig. 2, using an existing DEM and the InSAR imaging geometry for the interferometric pair (Fig. 2). Removing the topographic effects (Fig. 4a+4b) from the original one (Fig. 2) results in an interferogram containing the ground surface deformation during the time duration and the measurement noise (Fig. 4c+4d),

$$\phi_{def} = \phi - \phi_{dem} \quad (8)$$

If h is taken as zero, the procedure outlined in Equations 5-8 will remove the effect of an ellipsoidal earth surface on the interferogram. This results in a flattened interferogram, where the phase value can be mathematically approximated as

$$\phi_{flat} = -\frac{4\pi}{\lambda}\frac{B\cos(\theta_1 - \alpha)}{r_1 \sin\theta_1}h + \phi_{def} \quad (9)$$

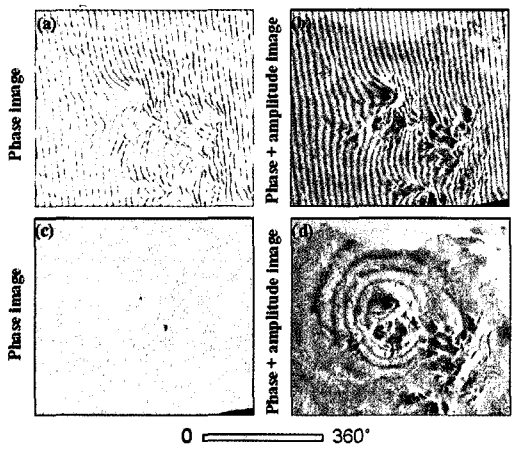

Fig. 4. (a, b) An interferogram that is simulated to represent the topographic contribution in the original interferogram (Figure 2). (c, d) Topography-removed interferogram by subtracting the interferograms in (a+b) from the original interferogram in Figure 2. Each interferometric fringe (full color cycle) represents 360° of phase change (or 2.83 cm of range change between the ground and the satellite).

$$= -\frac{4\pi}{\lambda}\frac{B_\perp}{H\tan\theta_1}h + \phi_{def}$$

where $B_\perp$ is the perpendicular component of the baseline with respect to the incidence angle θ_1 (Fig. 3). If ϕ_{def} is negligible, the phase value in Equation 9 can be used to calculate height h. This explains how InSAR can be used to produce an accurate, high-resolution DEM over a large region. For the ERS-1/-2 satellites, H is about 800 km, θ_1 is about $23^\circ \pm 3^\circ$, λ is 5.66 cm, and $B_\perp$ should be less than 1100 m for a coherent interferogram. Therefore, Equation 10 can be approximated as

$$\phi_{flat} \approx -\frac{2\pi}{9600}B_\perp h + \phi_{def} \qquad (10)$$

For an interferogram with $B_\perp$ of 100 m, 1 meter of topographic relief produces a phase value of 4°. However, producing the same phase value requires only 0.3 mm of surface deformation. Therefore, the interferogram phase value is much more sensitive to changes in topography (i.e., the surface deformation ϕ_{def}) than to the topography itself (i.e., h). That explains why repeat-pass InSAR is capable of detecting surface deformation at a theoretical accuracy of sub-centimeters.

The final procedure in 2-pass InSAR is to rectify the SAR images and interferograms into a map coordinate, which is a backward transformation of Equation 5. The geo-referenced interferogram (Fig. 5) and derived products can be readily overlaid with other data layers to enhance the utility of the interferograms and facilitate data interpretation. Fig. 5 shows 6 concentric fringes that represent about 17 cm of range decrease (mostly uplift)

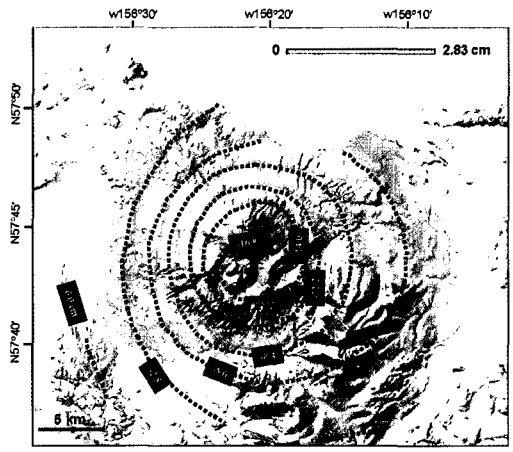

Fig. 5. A geo-referenced interferogram overlaid over a shaded relief image produced from a DEM. Each fringe corresponds to 2.8 cm of range change. The concentric pattern indicates ~17 cm of uplift centered on the southwest flank of Mount Peulik volcano, Alaska, which occurred during an inflation aseismic episode from October 1996 to September 1998 [Lu *et al.*, 2002c].

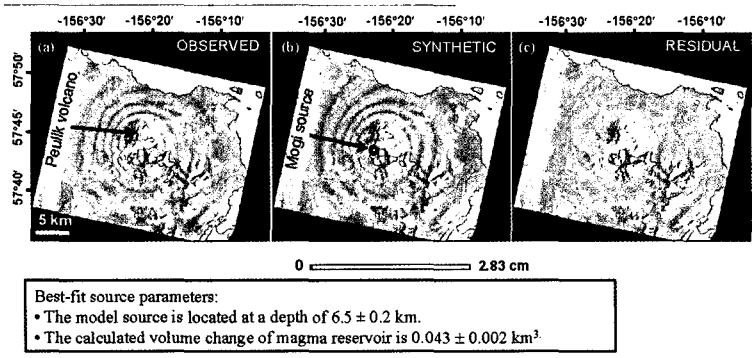

Fig. 6. Deformation interferograms (observed, modeled, and residual) for Mount Peulik volcano. Each fringe (full color cycle) represents 2.83 cm of range change between the ground and the satellite. Synthetic interferograms were produced using a best-fit inflationary point source at about 6.5 km depth with a volume change of 0.043 km^3. The residual interferogram is the difference between the observed and modeled interferograms. Areas of loss of radar coherence are uncolored.

centered on the southwest flank of Mount Peulik, Alaska. The volcano inflated aseismically from October 1996 to September 1998, a period that included an intense earthquake swarm, starting in May 1998, near Becharof Lake, 30 km northwest of Mount Peulik (Lu *et al.*, 2002c).

3. Interferogram Interpretation and Modeling

To understand the magmatic processes, numerical models are often employed to invert the physical parameters based on the observed deformation. The spatial resolution of surface displacement data provided by InSAR makes it possible to constrain models of volcanic deformation with a variety of source geometries such as the spherical point pressure source (Mogi source) (Mogi, 1958), the dislocation source (sill or dike source) (Okada, 1985), etc. Among the physical parameters, location and volume change of the magma reservoir are the most important ones.

The most widely used source in volcano deformation modeling is the spherical point pressure source (also called Mogi source) embedded in an elastic homogeneous half-space (Mogi, 1958). Even though Mogi source is the simplest, it can fit observed deformation data remarkably well. The four parameters used to describe the point source are horizontal location coordinates, depth, and volume change of a presumed magma body which is calculated by assuming the injected magma has the same elastic properties as the country rocks (Delaney and McTigue, 1994; Johnson *et al.*, 2000). The point source approximation is valid if the size of the source dimension is much smaller than its depth. A limitation of the half-space formulation is its neglect of topographic effects. To account for topographic effects, a simple approach proposed by Williams and Wadge (1998), in which the elevation of the reference surface varies according to the elevation of each computation point in the model, is normally adopted.

A nonlinear least-squares inversion approach is often used to optimize the source parameters (Press *et al.*, 1992; Cervelli, 2001). Inverting the observed interferogram in Fig. 5 using a Mogi source results in a best-fit source located at a depth of 6.5 $\pm$ 0.2 km. The calculated volume change is 0.043 $\pm$ 0.002 km^3. Fig. 6b shows the modeled interferogram based on the best-fit source parameters, and Fig. 6c is a residual interferogram that is the difference between the observed deformation (Fig. 6a) and modeled deformation (Fig. 6b). It is obvious that the Mogi source fits the observed deformation very well.

4. InSAR Stuidies of Alaskan Volcanoes

1) Introduction

Many volcanic eruptions are preceded by pronounced ground deformation in response to increasing pressure from magma chambers, or to the upward intrusion of magma (Dvorak and Dzurisin, 1997). In general, it is expected that a volcano is subject to inflation prior to an eruption, in which case magma migrates from depth, causing localized inflation. Subsequent eruption causes deflation as some or all of this magma is erupted to the surface. Analysis of surface deformation associated with eruptions or intrusions, along with seismicity and other information, provide significant inputs for studying magma dynamics.

The Alaskan volcanoes compromise roughly ten percent of the world's active volcanoes (Fig. 7). Major volcanic eruptions are annual events in the Aleutian arc. More than 170 eruptions were recorded in this area during the last 100 years. Although the rate of eruptive

activities in the Aleutian arc is very high, these volcanoes remain relatively poorly studied due to their remote locations, difficult logistics, high cost of field measurement, and persistent cloud cover. Therefore the all-weather radar satellite images with the capability of measuring subtle ground surface deformation can significantly improve our understanding of activity at these volcanoes. The following sections summarize our on-going investigations of Alaskan volcanoes with SAR images acquired from European ERS-1 and ERS-2, Canadian Radarsat-1, and Japanese JERS-1 satellites.

2) New Trident Volcano

The first application of InSAR to study surface deformation over the Aleutians was for the New Trident volcano (Fig. 7) that last erupted in 1963. An ERS-1 interferogram indicated about 7-9 cm of uplift from 1993 to 1995 (Lu *et al.*, 1997). Numerical modeling suggested inflation of a magma body located about 2 km beneath the volcano. Shortly thereafter, Alaska Volcano Observatory (AVO) geologists noted signs of dome-like uplift and fumarolic activity at New Trident (J. Freymueller, pers. comm., 1997).

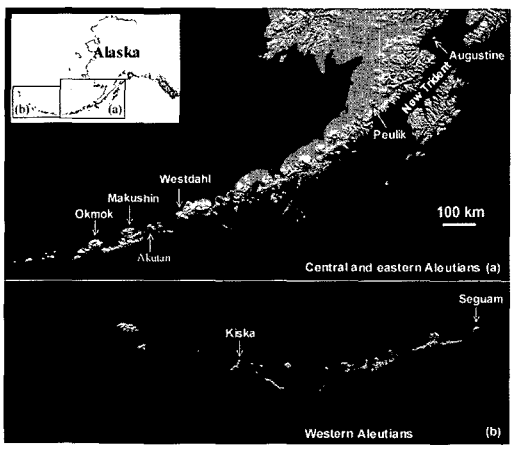

Fig. 7. Location map showing the Alaska volcanoes discussed in this paper. The volcanoes presented in this study spread over the central and eastern Aleutian islands (a) and western Aleutian islands (b).

3) Okmok Volcano

Okmok volcano (Fig. 7), a broad shield topped with a 10-km-wide caldera, produced blocky, basaltic flows during relatively large, effusive eruptions in 1945, 1958 and 1997 (Miller *et al.*, 1998). Multiple InSAR images mapped 1) surface inflation of more than 18 cm during 1992-1995 and subsidence of 1-2 cm during 1995-1996, prior to the 1997 eruption; 2) more than 140 cm of surface deflation during the 1997 eruption (Fig. 8a); and 3) 5-15 cm/year inflation during 1997-2003, after the 1997 eruption. Numerical modeling suggested the magma reservoir responsible for the observed deformation resided at a depth of about 3 km beneath the center of the caldera and about 5 km away from the eruptive vent. This example demonstrates how InSAR is capable of measuring pre-eruptive, co-eruptive, and post-eruptive deformation in the sub-arctic environment (Lu *et al.*, 1998b; Lu *et al.*, 2000a; Lu *et al.*, 2003a; Lu *et al.*, 2005a).

4) Akutan Volcano

Akutan volcano (Fig. 7), the second most active volcano in Alaska, was shaken in March 1996 by an intense earthquake swarm accompanied by extensive ground cracking but with no eruption of the volcano. On the western part of the island both L-band JERS-1 and C-band ERS-1/2 InSAR images show an uplift of as much as 60 cm that was associated with the swarm. The JERS interferogram (Fig. 8b), displays greater coherence, especially in areas with loose surface material or thick vegetation where C-band interferograms lose coherence, and also shows subsidence of a similar magnitude on the eastern part of the island, as well as displacements along faults that were reactivated during the seismic swarm. The axis of uplift and subsidence strikes about N70°W and is roughly parallel to 1) a zone of fresh cracks on the volcano's northwest flank, 2) normal faults that cut the island, and 3) the inferred maximum compressive stress

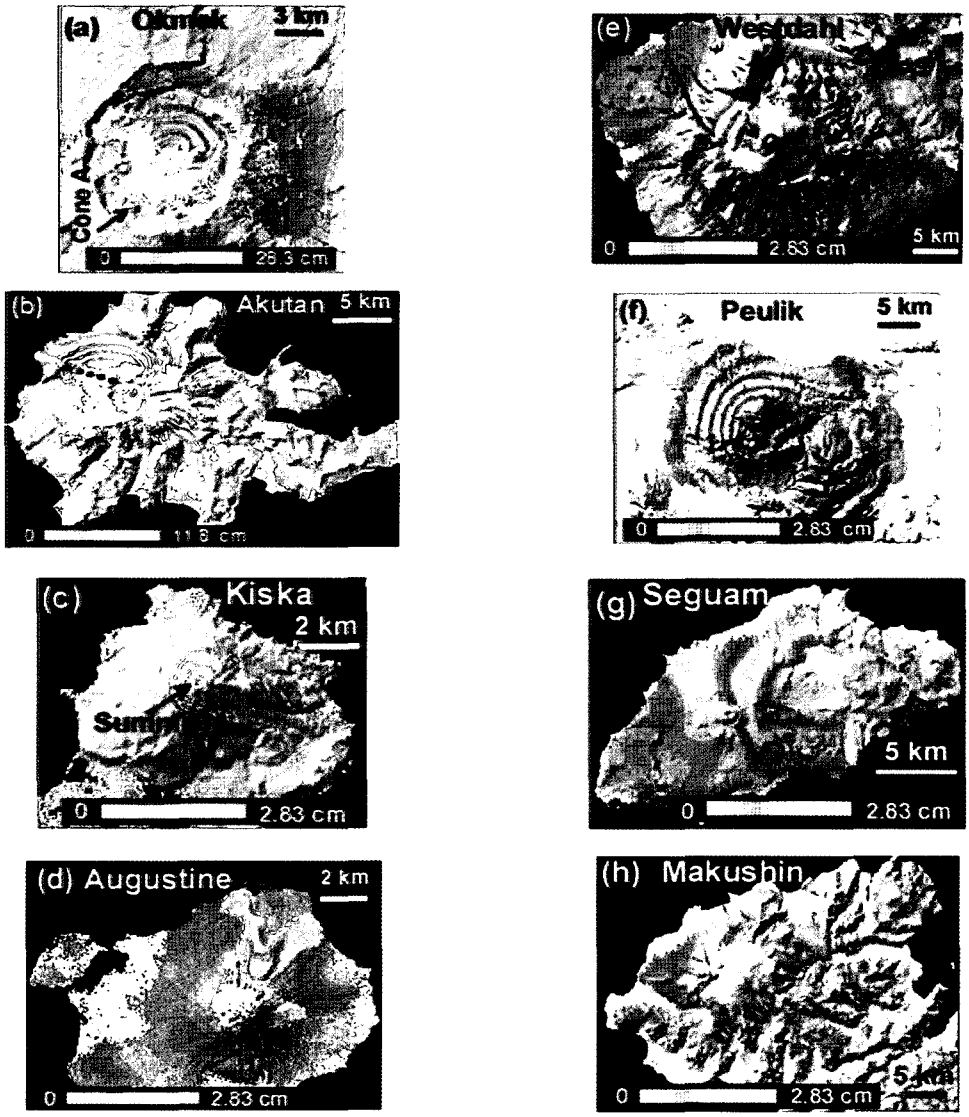

Fig. 8. (a) Deformation interferogram (Oct. 1995 - Sep. 1997), bracketing the Feb. - Apr. 1997 eruption of Okmok volcano, shows the volcano deflated more than 1.4 m due to magma withdrawal. The location of the 1997 vent, Cone A, is labeled. (b) Deformation interferogram of Akutan volcano, spanning the March 1996 seismic swarm, shows uplift of more than 60 cm on the western part of the island and subsidence of similar magnitude on the eastern part of the island. The dashed line represents a zone of ground cracks created during the 1996 seismic swarm. (c) Deformation interferogram for Kiska volcano shows subsidence of the volcano summit during Aug. 1999 and Aug. 2000. (d) Interferogram (1992-1993) of Augustine volcano depicts the subsidence associated with the compaction of the 1986 pyroclastic flow deposits outlined by the white dashed line. (e) An InSAR image (1993-1998) shows aseismic inflation of Westdahl volcano. The circle represents the horizontal position of the shallow magma reservoir beneath the Westdahl Peak. (f) Interferogram (Oct. 1996 - Oct. 1997) shows about 17 cm of uplift of Peulik volcano. The aseismic inflation occurred before the May 1998 earthquake swarm about 30 km northwest of the volcano. (g) Interferogram of Makushin volcano shows about 7 cm inflation associated with a possible eruption in Jan. 1995. (h) Interferogram of Seguam volcano shows uplift of the island from Jul. 1999 to Sep. 2000. All these interferograms are draped over the DEM shaded relief images and areas without interferometric coherence are uncolored.

direction. Both before and after the swarm, the northwest flank was uplifted 5-20 mm/year relative to the southwest flank, probably by magma intrusion. This example demonstrates that InSAR can provide a basis not only for interpreting and modeling movement of shallow magma bodies that feed eruptions, but also for detecting intrusive activities that do not result in an eruption (Lu *et al.*, 2000b; Lu *et al.*, 2005b).

5) Kiska Volcano

Kiska volcano (Fig. 7) is the westernmost, historically active volcano in the Aleutian arc. Sequential InSAR images of Kiska show a circular area, about 3 km in diameter and centered near the summit, that has subsided by as much as 10 cm from 1995 to 2001, mostly during 1999 and 2000 (Fig. 2c). Based on the shallow source depth (< 1 km), the copious amounts of steam that were vented during recent eruptions, and recent field reports of vigorous steaming and persistent ground shaking near the summit area, the observed subsidence is attributed to decreased pore-fluid pressure within a shallow hydrothermal system beneath the summit area (Lu *et al.*, 2002a).

6) Augustine Volcano

Augustine volcano (Fig. 7), an 8 by 11-km island, underwent six significant eruptions in the last two centuries: 1812, 1883, 1935, 1963-64, 1976, and 1986. InSAR images show the pyroclastic flows from the 1986 eruption have been experiencing subsidence/ compaction at a rate of about 3 cm per year (Fig. 8d) but no sign of significant volcano-wide deformation was observed during 1992-2000. The observed deformation can be used to study the characteristics of the pyroclastic flows (Lu *et al.*, 2003c; Masterlark *et al.*, 2004b).

7) Westdahl Volcano

Westdahl volcano (Fig. 7), a young glacier-clad shield volcano was frequently active during the latter half of the 20th century with documented eruptions in 1964, 1978-79, and 1991-92 (Miller *et al.*, 1998; Lu *et al.*, 2004). The background level of seismic activity since the last eruption was generally low (about five M < 3 earthquakes per year). InSAR images during 1991-2000 show that Westdahl volcano deflated during its 1991-92 eruption and is re-inflating at a rate that could produce another eruption in the next several years (Fig. 8e). The rates of post-eruptive inflation and co-eruptive deflation are approximated by exponential decay functions with time constants of about 6 years and a few days, respectively. This behavior is consistent with a deep, constant-pressure magma source connected to a shallow reservoir by a magma-filled conduit where the magma flow rate is governed by the pressure gradient between the deep source and the shallow reservoir. This example demonstrates that 1) InSAR is becoming the best tool available for detecting deep, aseismic magma accumulation by measuring broad, subtle deformation of the ground surface to identify restless volcanoes long before they become active and before seismic and other precursors emerge, and 2) multiple-temporal InSAR images enable construction of a virtual magma plumbing system that can be used to constrain models of magma accumulation in the shallow reservoir and shed light on the time window of the next eruption (Lu *et al.*, 2004; Lu *et al.*, 2000c; Lu *et al.*, 2003b).

8) Peulik Volcano

Peulik volcano (Fig. 7), a stratovolcano located on the Alaska Peninsula, is known to have erupted in 1814 and 1852 (Miller *et al.*, 1998). InSAR images that collectively span the time interval from July 1992 to August 2000 reveal that a presumed magma body located 6.6 km beneath the Peulik volcano inflated 0.051 km^3 between October 1996 and September 1998. The average inflation rate of the magma body was about 0.003 km^3/month from October 1996 to September 1997 (Fig. 8f), peaking at 0.005 km^3/month during June

26-October 9, 1997, and dropping to 0.001 km^3/month from October 1997 to September 1998. Deformation before October 1996 or after September 1998 was not significant. An intense earthquake swarm occurred about 30 km northwest of Peulik from May to October, 1998, around the end of the inflation period. The 1996-98 inflation episode at Peulik confirms that InSAR can be used to detect magma accumulation beneath dormant volcanoes at least several months before other signs of unrest are apparent. This application represents a first step toward understanding the eruption cycle at Peulik and other stratovolcanoes with characteristically long repose periods (Lu *et al.*, 2002c).

9) Seguam Volcano

Seguam volcano (Fig. 7), often referred to Pyre Peak, erupted in 1901, 1927, 1977, and 1992-1993 (Miller *et al.*, 1998). InSAR images, spanning various intervals during 1992-2000, document co-eruptive and post-eruptive deformation (Fig. 8g) of the 1992-1993 eruption. A model that combines magma influx, thermoelastic relaxation, and poroelastic effects accounts for the observed deformation. This example demonstrates that spatial and temporal coverage of the InSAR data can be used to reveal dynamic processes within a volcano (Lu *et al.*, 2003c; Masterlark and Lu, 2004a).

10) Makushin Volcano

Makushin volcano, a broad, ice-capped, truncated stratovolcano, is one of the more active volcanoes in the Aleutians, producing at least 17 explosive, relatively small eruptions since the late 1700s (Miller *et al.*, 1998). Additional smaller eruptions probably occurred during this period but were unrecorded, either because they occurred when the volcano was obscured by clouds or because the eruptive products did not extend beyond the volcano's flanks. Several independent InSAR images, that each span the time period from October 1993 to September 1995, show evidence of about 7 cm of uplift (Fig. 8h) centered on the volcano's east flank. The uplift was interpreted as pre-eruptive inflation of a small explosive, but unsubstantially reported eruption on January 30, 1995. This example demonstrates that ground deformation of a few cm can be unambiguously identified with InSAR images over a rugged terrain where geometric distortion of radar images is severe (Lu *et al.*, 2002b).

5. Conclusions

The satellite InSAR technique has proven to be a powerful space-borne geodetic tool for studying a variety of volcanic processes by analyzing surface deformation patterns (Lu *et al.*, 1997, 1998a, 1998b, 2000a, 2000b, 2000c, 2002a, 2002b, 2002c, 2003a, 2003b, 2003c, 2004, 2005a, 2005b). With the implementation of InSAR technology, volcano monitoring has entered an exciting phase wherein magma accumulation in the middle to upper crust can be observed long before the onset of short-term precursors to an eruption. Ultimately, more widespread use of InSAR for volcano monitoring could shed light on a part of the eruption cycle - the time period between eruptions when a volcano seems to be doing essentially nothing. This makes InSAR an excellent space-based, long-term volcano monitoring tool. Combining applications of the InSAR technique with observations from continuous GPS, gravity, strainmeters, tiltmeters, seismometers and volcanic gas studies will improve our capability to forecast future eruptions and will lead to improved volcano hazard assessments and better eruption preparedness.

Acknowledgments

ERS-1 and ERS-2, Radarsat-1, and JERS-1 SAR

images are copyrighted © 1991-2003 European Space Agency (ESA), Canadian Space Agency (CSA), and Japan Aerospace Exploration Agency (JAXA), respectively, and were provided by ASF, ESA, and JAXA. The research summarized in the paper was supported by funding from NASA Radarsat Program (NRA-99-OES-10 RADARSAT-0025-0056) and Solid Earth & Natural Hazards Program, USGS contracts O3CRCN0001 and 1434-CR-97-CN-40274, and USGS Land Remote Sensing Program and Volcano Hazards Program. We thank the ASF, JAXA and ESA staff members for their world-class services and special efforts in making the SAR data available to us on a timely basis. We also thank J. Freymueller, O. Kwoun, D. Mann, T, Masterlark, V. McConnell, D. Meyer, S. Moran, R. Rykhus, W. Thatcher and many other colleagues for contributions to this research.

References

Cervelli, P., M. H. Murray, P. Segall, Y. Aoki, and T. Kato, 2001. Estimating source parameters from deformation data, with an application to the March 1997 earthquake swarm of the Izu Peninsula, Japan, *J. Geophys. Res.*, 106(11): 217-11,237.

Curlander, J. and R. McDonough, 1991. *Synthetic aperture radar systems and signal processing*, New York: John Wiley & Sons.

Delaney, P. T. and D. F. McTigue, 1994. Volume of magma accumulation or withdrawal estimated from surface uplift or subsidence, with application to the 1960 collapse of Kilauea Volcano, *Bull. Volcanol.*, 56: 417-424.

Dvorak, J. and D. Dzurisin, 1997. Volcano geodesy: The search for magma reservoirs and the formation of eruptive vents, *Rev. Geophys.*, 35: 343-384.

Farr T. G. and M. Kobrick, 2000. Shuttle Radar Topography Mission produces a wealth of data, *Eos Trans.*, 81: 583-585.

Gabriel, A. K., R. M. Goldstein, and H. A. Zebker, 1989. Mapping small elevation changes over large areas: differential radar interferometry, *J. Geophys. Res.*, 94: 9183-9191.

Gray, A. L. and P. J. Farris-Manning, 1993. Repeat-pass interferometry with airborne synthetic aperture radar, *IEEE Transactions on Geoscience and Remote Sensing*, 31: 180-191.

Hanssen, R., 2001. *Radar interferometry: data interpretation and error analysis.* Netherlands: Kluwer Academic Publishers.

Johnson, D. J., F. Sigmundsson, and P.T. Delaney, 2000. Comment on "Volume of magma accumulation or withdrawal estimated from surface uplift or subsidence, with application to the 1960 collapse of Kilauea volcano" by P.T. Delay and D.F. McTigue, *Bull. Volcanol.*, 61: 491-493.

Lu, Z., R. Fatland, M. Wyss, S. Li, J. Eichelberger, K. Dean, and J. Freymueller, 1997. Deformation of New Trident volcano measured by ERS-1 SAR interferometry, Katmai national Park, Alaska, *Geophys. Res. Lett.*, 24: 695-698.

Lu, Z. and J. Freymueller, 1998a. Synthetic aperture radar interferometry coherence analysis over Katmai volcano group, Alaska, *Journal of Geophysical Research*, 103: 29887-29894.

Lu, Z., D. Mann, and J. Freymueller, 1998b. Satellite radar interferometry measures deformation at Okmok volcano, *EOS*, 79: 461-468.

Lu, Z., D. Mann, J. Freymueller, and D. Meyer, 2000a. Synthetic aperture radar interferometry of Okmok volcano, Alaska: Radar observations, *Journal of Geophysical Research*, 105: 10791-10806.

Lu, Z., C. Wicks, J. Power, and D. Dzurisin, 2000b.

Ground deformation associated with the March 1996 earthquake swarm at Akutan volcano, Alaska, revealed by satellite radar interferometry, *Journal of Geophysical Research*, 105: 21, 483-21, 496.

Lu, Z., C. Wicks, D. Dzurisin, W. Thatcher, J. Freymueller, S. McNutt, and D. Mann, 2000c. Aseismic inflation of Westdahl volcano, Alaska, revealed by satellite radar interferometry, *Geophysical Research Letters*, 27: 1567-1570.

Lu, Z., T. Masterlark, J. Power, D. Dzurisin, and C. Wicks, 2002a. Subsidence at Kiska volcano, Western Aleutians, Detected by Satellite Radar Interferometry, *Geophysical Research Letters*, 29(18), 1855, doi:10.1029/2002GL014948.

Lu, Z., J. Power, V. McConnell, C. Wicks, and D. Dzurisin, 2002b. Pre-Eruptive Inflation and Surface Interferometric Coherence Characteristics Revealed by Satellite Radar Interferometry at Makushin Volcano, Alaska: 1993 - 2000, *Journal of Geophysical Research*, 107(B11), 2266, doi:10.1029/2001JB000970.

Lu, Z., C. Wicks, D. Dzurisin J. Power, S. Moran, and W. Thatcher, 2002c. Magmatic Inflation at a Dormant Stratovolcano: 1996-98 Activity at Mount Peulik Volcano, Alaska, Revealed by Satellite Radar Interferometry, *Journal of Geophysical Research*, 107(B7), 2134, doi:10.1029/2001JB000471.

Lu, Z., E. Fielding, M. Patrick, and C. Trautwein, 2003a. Estimating Lava Volume by Precision Combination of Multiple Baseline Spaceborne and Airborne Interferometric Synthetic Aperture Radar: the 1997 Eruption of Okmok Volcano, Alaska, *IEEE Transactions on Geoscience and Remote Sensing*, 41(6): 1428-1436.

Lu, Z., T. Masterlark, D. Dzurisin, R. Rykhus, and C. Wicks, 2003b. Magma Supply Dynamics at Westdahl Volcano, Alaska, Modeled from Satellite Radar Interferometry, *Journal of Geophysical Research*, 108(B7), 2354, 10.1029/2002JB002311.

Lu, Z., C. Wicks, D. Dzurisin, J. Power, W. Thatcher, and T. Masterlark, 2003c. Interferometric synthetic aperture radar studies of Alaska volcanoes, *Earth Observation Magazine* (EOM), 12(3): 8-18.

Lu, Z., R. Rykhus, T. Masterlark, and K. Dean, 2004. Mapping recent lava flows at Westdahl volcano, Alaska, using radar and optical satellite imagery, *Remote Sensing of Environment*, 91: 345-353.

Lu, Z., T. Masterlark, and D. Dzurisin, 2005a. Interferometric Synthetic Aperture Radar (InSAR) Study of Okmok Volcano, Alaska, 1992-2003: Magma Supply Dynamics and Post-emplacement Lava Flow Deformation, *Journal of Geophysical Research*, vol. 110, B02403, DOI:10.1029/2004JB003148, in-press.

Lu, Z., C. Wicks, O. Kwoun, J. Power, and D. Dzurisin, 2005b. Surface deformation associated with the March 1996 earthquake swarm at Akutan Island, Alaska, revealed by C-band ERS and L-band JERS radar interferometry, *Canadian Journal of Remote Sensing*, 31(1): 7-20.

Massonnet, D., M. Rossi, C. Carmona, F. Adragna, G. Peltzer, K. Feigi, and T. Rabaute, 1993. The displacement field of the Landers earthquake mapped by radar interferometry, *Nature*, 364: 138-142.

Massonnet, D., P. Briole, and A. Arnaud, 1995. Deflation of Mount Etna monitored by spaceborne radar interferometry, *Nature*, 375: 567-570.

Massonnet, D., and K. Feigl, 1998. Radar interferometry and its application to changes in the Earth's surface, *Rev. Geophys.*, 36: 441-500.

Masterlark, T., and Z. Lu, 2004a. Transient volcano

deformation sources imaged with InSAR: Application to Seguam island, Journal of Geophysical Research, *J. Geophys. Res.* 109, B01401, doi:10.1029/2003JB002568.

Masterlark, T., Z. Lu, and R. Rykhus, 2004b. Thickness distribution of a cooling pyroclastic flow deposit: Optimization using InSAR, FEMs, and an adaptive mesh algorithm, *Journal of Volcanology and Geothermal Research*, accepted.

Miller, T.M., R.G. McGimsey, D.H. Richter, J.R. Riehle, C.J. Nye, M.E. Yount, and J.A. Dumoulin, 1998. Catalog of the historically active volcanoes of Alaska, *USGS Open-File Report*, pp.98-582.

Mogi, K., 1958. Relations between the eruptions of various volcanoes and the deformations of the ground surface around them, *Bull. Earthquake Res. Inst. Univ. Tokyo*, 36: 99-134.

Okada, Y., 1985. Surface deformation due to shear and tensile faults in a half-space, *Bull. Seismol. Soc. Am.*, 75: 1135-1154.

Press, W., S. Teukolsky, W. Vetterling, and B. Flannery, 1992. *Numerical recipes in C, the art of scientific computing*, Cambridge Univ. Press, 994 pp.

Rosen, P., S. Hensley, I.R. Joughin, F.K. Li, S.N. Madsen, E. Rodriguez, and R.M. Goldstein, 2000. Synthetic aperture radar interferometry, *Proceedings IEEE*, 88: 333-380.

Williams, C.A., and G. Wadge, 1998. The effects of topography on magma chamber deformation models: Application to Mt. Etna and radar interferometry, *Geophys. Res. Lett.*, 25: 1549-1552.

Zebker H. and others, 1992. The TOPSAR interferometric radar topographic mapping instrument, *IEEE Transactions on Geoscience and Remote Sensing*, 30: 933-940.

Zebker, H. A., P. A. Rosen, R. M. Goldstein, A. Gabriel, and C. L. Werner, 1994. On the derivation of coseismic displacement fields using differential radar interferometry: The Landers earthquake, *J. Geophys. Res.*, 99: 19617-19634.